Understanding Eddy Saturation in the Southern Ocean using Mean Field Theory

Joe Fitzgerald

August 16, 2015

Abstract

The winds over the Southern Ocean are increasing with time, and the impact that this change in forcing will have on the structure of the Antarctic Circumpolar Current (ACC) is not well understood. The statistical mean state of the ACC is set by a competition of several physical processes including the direct effects of winds, as well as the effects of eddies produced by baroclinic instability. We formulate a highly idealized two-layer quasi-geostrophic model of the ACC using a zonally-reentrant channel geometry. We determine the dependence of the equilibrium shear on the imposed wind stress in this model and find that some eddy saturation occurs: the domain mean eddy diffusivity is found to increase with increasing wind stress, mitigating the wind-driven tendency to steepen the interfacial slope. We then formulate the mean-field dynamics of our idealized model in which eddy-eddy interactions are discarded but eddy-mean flow interactions are retained. We find that the mean-field model robustly reproduces the qualitative dependence of the shear on wind stress seen in the full model. The mean-field model also captures the sense of the dependence of the full dynamics on other model control parameters such as the bottom friction. Our results suggest that mean-field dynamics constitutes a simplified and useful theoretical framework within which progress toward a physical understanding of eddy diffusion in the ACC might be made.

1 Introduction

The Antarctic Circumpolar Current (ACC) is a strong eastward current circulating around the Antarctic continent with surface speeds on the order of 30 cm/s and strong eastward flow extending to depth. The ACC is driven by persistent westerly winds blowing over the surface of the Southern Ocean (SO) with characteristic velocities on the order of 10 m/s, corresponding to a surface wind stress of approximately 0.2 N/m^2 [10]. The ACC is characterized by a strong vertical shear of zonal velocity, with the large surface currents diminishing to a weak flow near the ocean bottom. This vertical shear is associated with the sloping of isopycnal surfaces across the ACC: isopycnals deepen moving away from the Antarctic continent, with the rate of deepening being proportional to the strength of the zonal mean shear. The SO is zonally reentrant in the Drake Passage latitude band near

60S, but connects with the zonally-bounded ocean basins equatorward of the ACC. Isopycnals in the ocean basins are relatively flat and are continuous with those in the ACC. An emerging theoretical paradigm [14, 15] relates the depth of each isopycnal in the basin interior to the slope of that isopycnal across the ACC. In this picture, isopycnal slopes in the ACC play an important role in setting the deep stratification of the ocean basins. The deep stratification in turn influences the large-scale meridional overturning circulation in the Atlantic basin, which largely flows along isopycnal surfaces. The overturning circulation redistributes carbon and heat on the planetary scale and thus plays a critical role in global climate [10]. These considerations indicate that understanding the physical processes controlling the strength and vertical structure of the ACC constitutes an important problem in climate dynamics.

Observational records indicate that the strength and structure of the winds over the SO are changing in time. These changes have been linked to Antarctic ozone depletion, and have led to stronger eastward surface winds at ACC latitudes [19, 20]. How the ACC will respond to this change in forcing is not well understood. Observational results have suggested that the SO carbon sink is weakening as a result of the wind increases due to an associated enhancement of the upwelling rate in the SO [8]. Some theoretical arguments [15] connect such increases in upwelling with steepening of ACC isopycnal slopes. However, observations have also suggested that isopycnal slopes in the ACC have remained essentially constant [3], and high-resolution numerical modeling results have recently demonstrated that SO overturning rate and isopycnal slopes may not covary as suggested by theoretical models [12].

The spatial structure of the zonal mean isopycnals in the depth-latitude ACC cross-section are determined by the interactions of several physical processes. These processes include the surface buoyancy fluxes, which set the buoyancy structure in the outcrop region; the surface Ekman transport, which tends to steepen isopycnals in the ACC region; and heat fluxes due to baroclinic eddies, which act to flatten isopycnals. Surface buoyancy fluxes are commonly taken to be constant in theoretical models of the ACC, although this assumption has been shown to have important impacts on the response of the overturning as winds are increased [2]. The Ekman response is well-understood and increases linearly with the imposed wind stress. The eddy response is less straightforward, and understanding how eddy effects vary with forcing constitutes a crucial step toward understanding the large scale stratification and overturning of the world oceans.

Recent work has shown that numerical model predictions of the response of the ACC mean state to changes in wind forcing is strongly dependent on how eddies are treated in those models. Coarse resolution simulations typically parameterize eddies using the Gent-McWilliams scheme and predict that the overturning and isopycnal slopes will respond strongly to increases in the wind stress [14, 15]. In contrast, high resolution simulations that permit or resolve eddies in the SO have predicted a dramatically reduced sensitivity of isopycnal slopes to increasing winds [13]. This reduction in sensitivity associated with the accurate simulation of SO eddies is referred to as eddy-saturation, and can produce isopycnal slopes that are entirely independent of wind stress in some cases.

The effects of eddies on the SO mean state are frequently studied using the theoretical framework of the transformed Eulerian mean (TEM) [9, 7]. The TEM description of the relationship between eddies, winds, and isopycnal slopes is typically phrased as follows

(following [2]). The steady-state Eulerian zonal mean budget buoyancy budget is

$$\overline{v}\partial_y\overline{b} + \overline{w}\partial_z\overline{b} + \partial_y\overline{v'b'} + \partial_z\overline{w'b'} = \mathcal{D} \tag{1}$$

in which (y, z) are the meridional and vertical Cartesian coordinates, (v, w) are the velocity components in the y and z directions, b is the buoyancy, $\mathcal{D}$ represents any diabatic forcing terms, and overbars and primes are used to indicate the zonal mean and deviations from the zonal mean. Defining the TEM eddy streamfunction by $\psi^\star = -\overline{w'b'}/\partial_y\overline{b}$, (1) can be rewritten as

$$J(\psi_{\text{res}}, \overline{b}) = \mathcal{D} - \partial_y\left[(1-\mu)\overline{v'b'}\right]. \tag{2}$$

Here we use the Jacobian notation $J(f, g) = \partial_y f\partial_z g - \partial_z f\partial_y g$ and have defined the quantities $\psi_{\text{res}} = \overline{\psi} + \psi^\star$ and $\mu = -(\partial_z b)\overline{w'b'}/(\partial_y\overline{b})\overline{v'b'}$, where $\overline{\psi}$ is the streamfunction corresponding to the Eulerian mean velocities $\overline{v}$ and $\overline{w}$. If the eddies act adiabatically so that their heat fluxes are aligned with isopycnals then $\mu = 1$ and in the absence of explicit diabatic terms we obtain

$$J(\psi_{\text{res}}, \overline{b}) = 0. \tag{3}$$

This result shows that the residual circulation, which is the circulation relevant to heat transport, is along isopycnals in an adiabatic ocean.

Many idealized models of the ACC are formulated in the geometry of a zonally-reentrant channel bounded by zonal walls. In such a model isopycnals will intersect the wall on the equatorward side, which constrains the residual circulation to vanish. This is because ψ_{res} vanishes on the boundary by the condition of no normal flow at the wall, and ψ_{res} is constant along isopycnals by (3). If $\mu = 0$ we can rewrite the eddy streamfunction as $\psi^\star = \overline{v'b'}/\partial_z\overline{b}$ and the condition of zero residual circulation gives

$$0 = \overline{\psi} + \psi^\star = \overline{\psi} + \frac{\overline{v'b'}}{\partial_z\overline{b}}. \tag{4}$$

The Eulerian mean streamfunction is given by the well-known Ekman overturning $\overline{\psi} = -\tau/(\rho_0 f)$ where τ is the surface wind stress, ρ_0 is a reference density and f is the Coriolis parameter. Assuming a Gent-McWilliams-like flux-gradient form for the eddy heat flux $\overline{v'b'} = -K\partial_y\overline{b}$ in (4) immediately yields the formula

$$s = -\frac{\partial_y\overline{b}}{\partial_z\overline{b}} = \frac{\tau}{\rho_0 f K} \tag{5}$$

which predicts the isopycnal slope s in terms of the external parameters τ, f, and ρ_0 as well as the eddy diffusion coefficient K. Although the real ACC is not bounded by zonal walls, it remains plausible that (5) holds at leading order, as observations of the SO indicate that the residual circulation is much weaker than either the eddy or Eulerian mean streamfunctions, implying that the two contributions to ψ_{res} cancel one another heavily [10].

Equation (5) summarizes the competing effects of winds and eddies in determining the isopycnal slopes. Increasing the wind stress τ steepens isopycnals according to the Ekman response, while strengthening the eddy fluxes by increasing K flattens isopycnals. If K is taken to be a constant, increasing τ produces a linear increase in the slope. On the other hand, if K is taken to be proportional to the wind stress, then s will be invariant

to changes in τ, i.e., the ACC will be completely eddy saturated. No accepted theoretical argument currently exists to predict K, and many different assumptions have been used to parameterize K and obtain a scaling for $s(\tau)$. Marshall and Radko [9] took K to be proportional to the isopycnal slope $K = \alpha s$ to obtain $s \sim \sqrt{\tau}$. Based on mixing-length arguments, Abernathey and Marshall [2] related K to the eddy kinetic energy (EKE) as $K \sim \sqrt{\text{EKE}}$. In their simulations EKE was found to depend linearly on τ, predicting $K \sim \sqrt{\tau}$. Meredith et al. [11] also suggested that K scales with EKE, but according to a more complex relationship having two limiting cases. In the limit of small EKE, they obtain $K \sim \text{EKE}^{3/2}$, while in the limit of large EKE they obtain $K \sim \sqrt{\text{EKE}}$. Assuming $\text{EKE} \sim \tau$, these results predict a family of scaling laws $s \sim \tau^\gamma$ with $-1/2 < \gamma < 1/2$. This range of scalings includes cases in which isopycnal slopes steepen with τ, are constant with τ, or decrease with τ.

Based on the above discussion it is clear that an improved understanding of eddy physics in the ACC is required to make progress on the problem of the SO response to changes in forcing. In this work, we use the two-layer quasigeostrophic (QG) equations to formulate a highly-idealized model of the ACC. Within the context of this model, we identify a reduced set of dynamics, the mean-field dynamics, which appears to reproduce the dependence of the mean state on the winds that we observe in the full dynamics. The mean-field dynamics is obtained by discarding eddy-eddy interactions from the full nonlinear equations of motion while retaining the interactions between the eddies and the mean flow. This approach has previously been successful in a variety of applications. O'Gorman and Schneider [16] applied mean-field theory to an atmospheric GCM and obtained a mean state and storm track statistics similar to those of the unapproximated GCM. Mean-field theory has also been successful in predicting the formation and structure of zonal jets emerging on the stochastically-driven barotropic β-plane [4, 17]. It is hoped that our application of the highly-simplified mean-field dynamics to the ACC will provide a more tractable theoretical framework within which progress toward understanding the eddy response to wind stress variations may be made in the future.

2 Model Formulation

2.1 Model Geometry and Equations of Motion

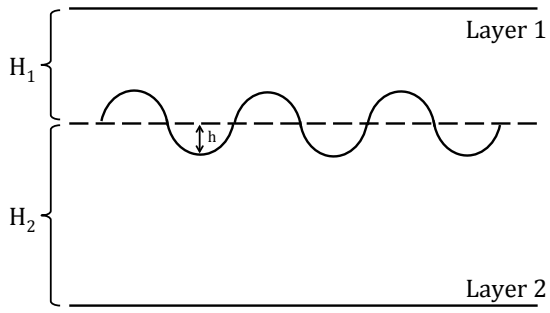

Figure 1: Schematic (x, z) cross-section of the two-layer model geometry.

We consider the motion of two fluid layers with thicknesses

$$h_1 = H_1 + h \tag{6}$$
$$h_2 = H_2 - h \tag{7}$$

where H_1 and H_2 are the (constant) mean thicknesses of layers 1 and 2 and $h(x, y, t)$ is the excess thickness of layer 1. We take x (increasing eastward) and y (increasing equatorward) to be our zonal and meridional coordinates on a zonally-reentrant β-plane channel of meridional width W and zonal extent L. A cross section of the model geometry is illustrated in Fig. 1. The local slope of the interface between the two layers is given by the gradient of h and is the analog of the isopycnal slope in the two-layer case. In the QG approximation, the dynamics of the two layers are formulated in terms of the upper and lower layer QG potential vorticities (PVs) q_1 and q_2, which are defined as

$$q_1 = \boldsymbol{\nabla}^2\psi_1 + \beta y - F_1(\psi_1 - \psi_2) \tag{8}$$
$$q_2 = \boldsymbol{\nabla}^2\psi_2 + \beta y + F_2(\psi_1 - \psi_2). \tag{9}$$

Here ψ_1 and ψ_2 denote the upper and lower layer geostrophic streamfunctions, which are related to the geostrophic velocity components via $u_{1,2} = -\partial\psi_{1,2}/\partial y$ and $v_{1,2} = \partial\psi_{1,2}/\partial x$. As we work on the β-plane, $\beta = \mathrm{d}f/\mathrm{d}y$ is a constant parameter. The parameters F_1 and F_2 are defined in terms of the mean layer depths as

$$F_1 = \frac{f_0^2}{g'H_1} \qquad\qquad F_2 = \frac{f_0^2}{g'H_2} \tag{10}$$

in which f_0 is the constant background Coriolis parameter and g' is the reduced gravity $g' = g(\rho_2 - \rho_1)/\rho_2$ where ρ_i is the constant density of the fluid in layer i. We take $\rho_2 > \rho_1$ so that the fluid is stably stratified. The difference $\psi_1 - \psi_2$ appearing in (8,9) is related to the interface deflection h through the relation

$$f_0(\psi_1 - \psi_2) = g'h \tag{11}$$

so that the zonal mean interfacial slope is given by

$$s \equiv -\frac{\partial\overline{h}}{\partial y} = \frac{f_0}{g'}(U_1 - U_2) \tag{12}$$

in which the overbar indicates a zonal average and we denote the zonal mean flow by $U_{1,2} = \overline{u}_{1,2}$. Note the negative sign in the definition of s: as h is the excess thickness in layer 1, $s < 0$ corresponds to h increasing with y. Equation (12) relates the baroclinic component of the mean flow to the interfacial slope, and indicates that for positive shear $U_1 > U_2$ the interface deepens as we move equatorward ($f_0 < 0$).

The PV fields evolve according to the dynamical equations

$$\partial_t q_1 + J(\psi_1, q_1) = -r(q_1 - \beta y) - \frac{1}{\rho_1 H_1}\partial_y\tau + \kappa\boldsymbol{\nabla}^2 q_1 \tag{13}$$
$$\partial_t q_2 + J(\psi_2, q_2) = -r(q_2 - \beta y) - dF_2\boldsymbol{\nabla}^2\psi_2 + \kappa\boldsymbol{\nabla}^2 q_2 \tag{14}$$

in which $J(f,g) = (\partial_x f)(\partial_y g) - (\partial_y f)(\partial_x g)$. Conservation of PV in (13) and (14) is modified by forcing, in the form of wind stress acting on layer 1, and by dissipation, in the form of Rayleigh drag, diffusion, and bottom friction. We take the wind stress to be of the idealized form

$$\frac{1}{\rho_1 H_1}\tau(y) = A\sin(l_g y) \tag{15}$$

where $l_g = \pi/W$ and A controls the strength of the forcing. The stress is thus zonally-symmetric with a half-sinusoidal profile across the channel, and acts to drive eastward flow in the channel. Rayleigh drag damps the dynamical part of the PV $q_i - \beta y$ in both layers with coefficient r. This Rayleigh drag on PV derives from Rayleigh drag on the upper and lower layer velocities as well as on the interface deflection h, all with equal coefficients. Bottom friction acts only on the relative vorticity in layer 2. We take the drag coefficient to be dF_2 so that d controls the strength of the bottom drag when F_2 is held constant. Diffusion of PV with coefficient κ is included for numerical stability of the mean-field dynamics, which we introduce in Section 2.5. We set $\kappa = 0$ when working with the full nonlinear equations of motion, and so we ignore diffusion when discussing the full dynamics.

The model boundary conditions are periodic in x and appropriate boundary conditions are applied in the meridional direction to ensure mass conservation. Mass conservation requires that the meridional velocity vanishes at the boundaries $y = 0, W$, including both the geostrophic (v) and ageostrophic (v_a) parts of the meridional velocity. Since $\overline{v}_i = \overline{\partial\psi_i/\partial x} = 0$, the $v_i = 0$ geostrophic condition implies that $v_i' = 0$, where the prime denotes the deviation from the zonal mean. The ageostrophic condition $v_{ai} = 0$ implies the boundary condition $U_1 = U_2 = 0$ on the zonal mean zonal flow, which we discuss in Section 2.2. Free-slip boundary conditions are applied to u_i'.

2.2 Zonal Mean Dynamics and Residual Circulation

Although the PV-evolution equations (13,14) are sufficient to determine the dynamics, it is illuminating to examine the zonal mean dynamics directly in terms of the velocities and interface deflection. The zonal mean equations of motion for the interface and zonal flow are

$$\partial_t U_1 = \overline{v_1' q_1'} + f_0 \overline{v}_1^\dagger - rU_1 + \frac{1}{\rho_1 H_1}\tau \tag{16}$$

$$\partial_t U_2 = \overline{v_2' q_2'} + f_0 \overline{v}_2^\dagger - rU_2 - dF_2 U_2 \tag{17}$$

$$\partial_t \overline{h} = -\overline{w}^\dagger - r\overline{h} \tag{18}$$

in which we have defined the residual meridional velocities

$$\overline{v}_1^\dagger = \overline{v}_{1a} + \frac{1}{H_1}\overline{v_1' h'} \tag{19}$$

$$\overline{v}_2^\dagger = \overline{v}_{2a} - \frac{1}{H_2}\overline{v_2' h'} \tag{20}$$

$$\overline{w}^\dagger = \overline{w}_1 + \partial_y \overline{v_1' h'} = \overline{w}_2 + \partial_y \overline{v_2' h'}. \tag{21}$$

The second equality in (21) follows from continuity at the interface of the component of velocity normal to the interface, which ensures that h is a material surface viewed from

either fluid layer. Note that (11) implies $\overline{v_1' h'} = \overline{v_2' h'}$ and that mass continuity implies $\overline{v}_1^\dagger = -(H_2/H_1)\overline{v}_2^\dagger$. The vertical and meridional residual velocities are related through $H_1 \partial_y \overline{v}_1^\dagger = -H_2 \partial_y \overline{v}_2^\dagger = \overline{w}^\dagger$. Note that (18) implies that in steady state the residual circulation $\overline{w}^\dagger$ balances the diabatic effect of Rayleigh drag on the interface. The residual circulation in our simplified model is thus strongly constrained by the imposed drag parameters, and vanishes by necessity in the limit $r \to 0$.

The boundary condition of no normal flow at $y = 0, W$ places a constraint on the zonal mean flow at the walls that can be understood from (16). The PV flux $\overline{v_1' q_1'} = 0$ and thickness flux $\overline{v_1' h'}$ vanish at the walls because $v' = 0$ there, and $\tau = 0$ at the walls by our choice of forcing structure. The budget then becomes

$$\partial_t U_1 = f_0 \overline{v}_{1a} - r U_1. \tag{22}$$

We require that the ageostrophic meridional flow $\overline{v}_{1a} = 0$ at the walls to prevent a net flux of mass into or out of the layer. This implies that U_1 decays exponentially at the walls, and that if $U_1 = 0$ at $t = 0$, then $U_1 = 0$ for all time. Similar considerations apply to U_2. As described in Section 2.1, we take $U_1 = U_2 = 0$ at the channel walls as our boundary conditions on the mean flow.

The upper layer mean zonal momentum equation (16) shows that in the absence of eddies, Rayleigh drag, or time-dependence, the wind stress drives an equatorward residual flow $\overline{v}_1^\dagger > 0$ whose Coriolis force balances the stress. This is the representation of the Ekman response in our simplified two-layer model. The residual return flow $\overline{v}_2^\dagger$ in the lower layer produces an eastward Coriolis force that must be balanced by bottom friction on the zonal flow U_2, thereby requiring eastward flow $U_2 > 0$ in the lower layer. In the presence of eddies, the eddy PV fluxes $\overline{v_1' q_1'}$ and $\overline{v_2' q_2'}$ act to transfer momentum from the upper layer to the lower layer. It is straightforward to show that $H_1 \langle v_1' q_1' \rangle = -H_2 \langle v_2' q_2' \rangle$, where angle brackets denote a mean over the entire domain. This shows that the rate at which eddies remove momentum from the upper layer is equal to the rate at which they deposit momentum into the lower layer. Eddies produced by a baroclinically unstable shear then act to barotropize the flow, reducing the shear and flattening the interface.

We now use the zonal mean equations (16,17,18) to cast the eddy saturation argument discussed in the introduction into the language of our model. We make the assumption that diabatic effects are weak and that the residual circulation is unimportant. The steady state zonal mean momentum budgets then become

$$0 = \overline{v_1' q_1'} + \frac{1}{\rho_1 H_1} \tau \tag{23}$$

$$0 = \overline{v_2' q_2'} - d F_2 U_2. \tag{24}$$

Further assuming that the interface term in the potential vorticity is dominant over the planetary and relative vorticity terms, we write the PV fluxes in terms of the thickness flux as

$$\overline{v_1' q_1'} \approx -\frac{f_0}{H_1} \overline{v_1' h'} \tag{25}$$

$$\overline{v_2' q_2'} \approx +\frac{f_0}{H_2} \overline{v_2' h'} = \frac{f_0}{H_2} \overline{v_1' h'}. \tag{26}$$

Finally, we assume a flux-gradient relationship for the thickness flux

$$\overline{v_1' h'} = -K \frac{\partial \overline{h}}{\partial y}. \tag{27}$$

Combining expressions (23), (25), and (27) immediately yields an expression for the zonal mean interfacial slope s in terms of the model parameters and the eddy diffusivity K:

$$s = -\frac{\partial \overline{h}}{\partial y} = \frac{\tau}{f_0 \rho_1 K}. \tag{28}$$

Equation (28) implies that if the eddy diffusivity K is constant, the slope of the interface scales linearly with the imposed wind stress. On the other hand, if K is linear in the wind stress $K = \alpha\tau$, then the slope of the interface does not depend at all on the winds. This highlights the crucial role of eddies in determining the response of the ocean to changing forcing conditions.

The interfacial slope s is related to the zonal mean shear $U_1 - U_2$ by (12). By applying the flux-gradient relation to the zonal mean momentum budget of the lower layer, we can also obtain explicit formulas for U_1 and U_2 individually. Combining equations (26), (27), and (28) yields

$$U_2 = \frac{\delta}{dF_2} \frac{\tau}{\rho_1 H_1} \tag{29}$$

where $\delta = H_1/H_2$ is the ratio of layer depths. Writing $U_1 = U_2 + (U_1 - U_2)$ and applying (28) then yields

$$U_1 = \left(\frac{\delta}{dF_2} + \frac{1}{F_1 K} \right) \frac{\tau}{\rho_1 H_1}. \tag{30}$$

Equation (29) shows that, under these assumptions, the lower layer flow is independent of the eddy diffusivity K and is determined solely by the winds and bottom friction. The upper layer flow U_1 weakens with increasing K as larger eddy diffusivities correspond to a shallower interfacial slope and reduced vertical shear.

2.3 Model Fixed Point

As we are interested in the behavior of the model equations (13) and (14) as the wind stress forcing is varied, it is useful to determine whether stable fixed point solutions exist over some range of forcing strengths. The model indeed has a single, zonally-symmetric fixed point that is stable for sufficiently weak wind stress. The fixed point becomes baroclinically unstable as the wind stress is increased beyond a threshold value. For sufficiently strong winds, the flow in the channel is turbulent.

To obtain the fixed point in terms of the model parameters, we first write

$$\overline{q}_1 - \beta y = \hat{Q}_1 \cos(l_g y) \qquad \overline{q}_2 - \beta y = \hat{Q}_2 \cos(l_g y) \tag{31}$$

$$U_1 = \hat{U}_1 \sin(l_g y) \qquad U_2 = \hat{U}_2 \sin(l_g y) \tag{32}$$

so that the steady state, zonally-symmetric PV budgets become (from (13) and (14))

$$0 = -r\hat{Q}_1 \cos(l_g y) - \partial_y \left(A \sin(l_g y) \right) \tag{33}$$

$$0 = -r\hat{Q}_2 \cos(l_g y) - dF_2 \partial_y \left(-\hat{U}_2 \sin(l_g y) \right). \tag{34}$$

Equations (33) and (34) can be solved for the steady state values of U_1 and U_2 by writing the PV in terms of the zonal mean flow. We obtain

$$U_1\Big|_{FP} = A\frac{F_2 + l_g^2\left(1+\frac{F_2 d}{r}\right)}{F_2 d(l_g^2+F_1)+r(l_g^2+F_1+F_2)}\sin(l_g y) \tag{35}$$

$$U_2\Big|_{FP} = A\frac{F_2}{F_2 d(l_g^2+F_1)+r(l_g^2+F_1+F_2)}\sin(l_g y). \tag{36}$$

The corresponding upper and lower layer PV gradients are

$$\frac{\partial \overline{q}_1}{\partial y}\Big|_{FP} = \beta + \frac{l_g^2 A}{r}\sin(l_g y) \tag{37}$$

$$\frac{\partial \overline{q}_2}{\partial y}\Big|_{FP} = \beta - \frac{l_g^2 A}{r}\frac{dF_2^2}{dF_2(l_g^2+F_1)+r(l_g^2+F_1+F_2)}\sin(l_g y). \tag{38}$$

Several important theoretical properties of our model are revealed by expressions (35)-(38). From (35) and (36) it is clear that the fixed point values of U_1, U_2, and $U_1 - U_2$ all increase linearly with the wind stress A. Equations (35) and (36) also show that the fixed point structure depends crucially on the Rayleigh drag r. As $r \to 0$, the fixed point value of U_1 tends to infinity while U_2 asymptotes to a constant finite value. This can be understood from the zonal mean momentum and thickness budgets (16) and (18). In the absence of Rayleigh drag, (18) constrains the residual circulation to vanish. In the absence of a residual circulation, eddies, or Rayleigh drag in the momentum equation, (16) shows that the momentum injection by wind stress must be balanced by acceleration of the upper level flow. This argument illustrates that no fixed point exists for $r = 0$: the solution is always time-dependent, with the upper layer flow steadily increasing until the shear becomes baroclinically unstable, even for very weak wind forcing. The fixed point PV gradients (37) and (38) reveal the important role played by bottom drag in our model. The upper layer PV gradient is always positive, while the PV gradient in layer 2 is positive for small A and negative for sufficiently large A. However, if the coefficient of bottom friction $d \to 0$, the PV gradient in layer 2 can never become negative. As a change in sign of the PV gradient must occur somewhere in the domain as a necessary condition for baroclinic instability, this demonstrates that bottom drag is required for baroclinic instability to occur in this model. We discuss the stability of the fixed point in more detail in the next section.

2.4 Model Parameters and Instability Properties

The model dynamics depends on a number of parameters, whose values we choose to be approximately representative of the SO. As our primary interest is in the response of the model dynamics to changing wind stress, we will normally vary the strength of the wind stress A while keeping other parameters fixed. We also conduct a number of sensitivity tests by varying the damping parameters r and d. We hold the following parameters constant in

all model integrations:

$$W = 1000 \text{ km} \quad (39)$$
$$L = 2000 \text{ km} \quad (40)$$
$$F_1 = 5.5 \times 10^{-4} \text{ km}^{-2} \quad (41)$$
$$F_2 = 1.1 \times 10^{-4} \text{ km}^{-2} \quad (42)$$
$$\beta = 1.2 \times 10^{-3} \text{ (km day)}^{-1}. \quad (43)$$

The zonal extent of the channel is thus twice its meridional width. The ratio $F_1/F_2 = H_2/H_1 = 5$, so that the lower layer has a mean thickness of five times that of the upper layer. The model dynamics does not depend on the values of H_1 and H_2 outside their appearance in the F_1 and F_2 parameters. Similarly, the dynamics does not depend explicitly on g' or f_0. The Rossby deformation radius R_d is given by $R_d = (F_1 + F_2)^{-1/2} = 38.8$ km, so that our channel extends over 50 Rossby radii in the zonal direction and approximately 25 in the meridional direction. The value of β was chosen to represent a channel centered at 60°S.

It remains to specify the values of the drag parameters r, d, and κ, as well as the strength of the wind forcing A. We take a constant value of $\kappa = 20$ km^2/day in the mean-field dynamics and $\kappa = 0$ in the fully-nonlinear dynamics. The value of κ was chosen to be as small as possible while still allowing the numerical model to remain stable. The Rayleigh drag r and bottom drag d are varied in sensitivity tests, but our reference values are taken to be

$$r = 1 \times 10^{-4} \text{ day}^{-1} \quad (44)$$
$$d = 500 \text{ km}^2/\text{day}. \quad (45)$$

For the reference bottom friction value, the drag on the lower layer velocity has coefficient $dF_2 = 0.05$ day^{-1}, so that the bottom drag acts approximately 500 times more rapidly than the bulk Rayleigh drag. In the mean-field dynamics, the PV diffusion acts on the largest scales with coefficient $\kappa l_g^2 \sim 2 \times 10^{-4}$ day^{-1}. Diffusion in the mean-field model is thus twice as strong as the Rayleigh drag at the largest scales, and even stronger at smaller scales. Diffusion plays an important role in the mean field equations (due to numerical constraints) while playing no role in the nonlinear equations. This difference in dissipation constitutes a limitation of our results, and resolving this issue is an important future direction of this work. However, preliminary integrations of the nonlinear model in which comparable diffusion was added to the dynamics produced results similar to those without diffusion for wind stress values well beyond the stability boundary of the fixed point. This suggests that comparisons between the mean-field and nonlinear dynamics remain informative in spite of the differences in the dissipation properties of the two models.

We vary the wind stress over the range $A = 0.1 - 7.0$ km/day^2. We take as our reference value $A = 1$ km/day^2. In our notation the wind stress A appears directly as an acceleration of the zonal wind, and so has units of acceleration. To compare with realistic values of the wind stress over the SO it is conventional to write the acceleration as $\tau_0/(\rho_1 H_1)$ where τ_0 has units of stress (N/m^2) and ρ_1 is the density of the upper layer. Choosing as a typical density $\rho_1 \sim 1035$ kg/m^3 and an upper layer depth $H_1 \sim 1000$ m, our reference acceleration corresponds to a surface stress $\tau_0 \sim 0.14$ N/m^2. This is near the conventional

value of $\tau_0 = 0.2$ N/m^2, so that $A = 1$ km/day^2 is reasonably representative of the SO wind stress. By varying A over a wide range in the vicinity of this reference value, we assess how the state of the two-layer model ocean responds to changes in wind stress.

The growth rate of baroclinic instability is shown in Fig. 2 as a function of zonal wavenumber for $A = 1.0$ km/day^2 and reference values of the drag parameters. Panel (a) shows the growth rate in the nonlinear model ($\kappa = 0$) and panel (b) shows the growth rate in the mean-field dynamics ($\kappa = 20$ km^2/day). For this forcing value the fixed point is unstable with or without diffusion, and the e-folding time of the fastest growing wave is on the order of a few days. The growth rate peaks near zonal wavenumbers 4 and 5. The Rossby radius $Rd = 38.8$ km corresponds to a wavenumber $k_d \sim 1/R_d = .025$ km^{-1} which is near zonal wavenumber 8. Baroclinic instability thus sets in at scales somewhat larger than the Rossby radius. In the absence of diffusion the stable high wavenumbers decay on the timescale of the Rayleigh drag. With diffusion, all growth rates are reduced, and higher wavenumbers decay more rapidly. For $\kappa = 0$, instability sets in at a minimum wind strength of $A \sim .015$ km/day^2 for the reference drag values. For $\kappa = 20$ km^2/day, baroclinic instability does not set in until $A = 0.25$ km/day^2. As we vary A over the range $A = 0.1 - 7.0$ km/day^2, all model integrations are in the unstable regime for the nonlinear model diffusion. The mean-field model is stable for the first few wind stress values and unstable thereafter.

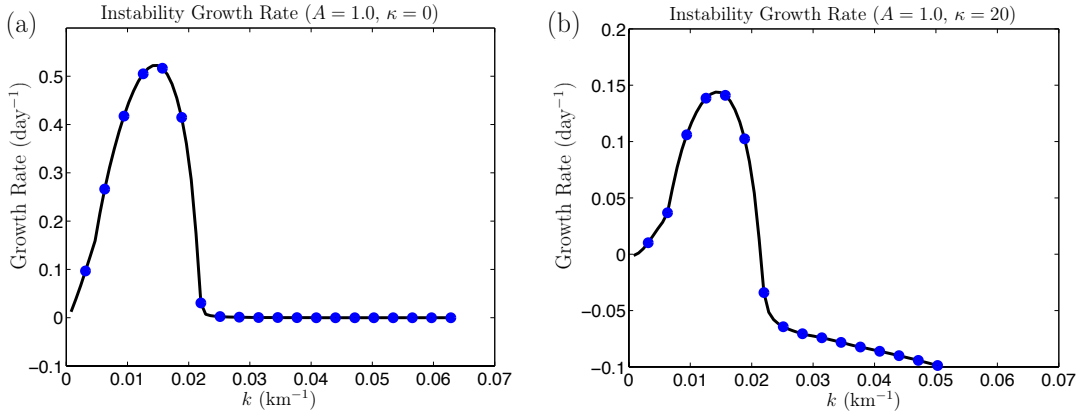

Figure 2: Growth rate of baroclinic instability as a function of wavenumber (a) without diffusion and (b) with diffusivity $\kappa = 20$ km^2/day. Blue circles indicate the quantized wavenumbers permitted by the periodic geometry. Reference values are used for all parameters.

2.5 Mean-Field Dynamics

Mean-field dynamics is a simplified theoretical model of the system (13,14) in which the nonlinearity associated with the advection of eddy quantities by the eddy velocity field is discarded but the nonlinearity associated with wave-mean flow interaction is retained. To derive the mean-field equations, we first rewrite the nonlinear equations of motion in the

Reynolds decomposition:

$$q_1 = \overline{q}_1 + q_1' = Q_1(y,t) + q_1'(x,y,t) \tag{46}$$
$$q_2 = \overline{q}_2 + q_2' = Q_2(y,t) + q_2'(x,y,t). \tag{47}$$

The mean PV fields Q_1 and Q_2 evolve according to the dynamical equations

$$\partial_t Q_1 = -\partial_y \overline{v_1' q_1'} - r\,(Q_1 - \beta y) - \frac{1}{\rho_1 H_1}\partial_y \tau + \kappa \partial_{yy} Q_1 \tag{48}$$
$$\partial_t Q_2 = -\partial_y \overline{v_2' q_2'} - r\,(Q_2 - \beta y) - dF_2 \partial_{yy}\overline{\psi}_2 + \kappa \partial_{yy} Q_2. \tag{49}$$

These equations are equivalent to the set of equations (16,17,18) except that we include the diffusion term for numerical stability of the approximated equations derived in what follows. The eddy PV fields q_1' and q_2' evolve according to

$$\partial_t q_1' = -U_1 \partial_x q_1' - v_1' \partial_y Q_1 - r q_1' + \kappa \boldsymbol{\nabla}^2 q_1' + \mathrm{EENL}_1 \tag{50}$$
$$\partial_t q_2' = -U_2 \partial_x q_2' - v_2' \partial_y Q_2 - r q_2' + \kappa \boldsymbol{\nabla}^2 q_2' - dF_2 \boldsymbol{\nabla}^2 \psi_2' + \mathrm{EENL}_2. \tag{51}$$

Here we use the notation EENL to denote the eddy-eddy nonlinearities, given by

$$\mathrm{EENL}_1 = -\partial_y \left(v_1' q_1' - \overline{v_1' q_1'} \right) - \partial_x \left(u_1' q_1' - \overline{u_1' q_1'} \right) \tag{52}$$
$$\mathrm{EENL}_2 = -\partial_y \left(v_2' q_2' - \overline{v_2' q_2'} \right) - \partial_x \left(u_2' q_2' - \overline{u_2' q_2'} \right). \tag{53}$$

Equations (48)-(51) are exact. To form the mean field equations, we simply drop the EENL terms, thereby discarding the effects of eddies advecting eddies. The discarded EENL terms are those responsible for the scattering of energy between different zonal wavenumber components of the flow. In the mean-field approximation, the dynamics is that of wave-mean flow interaction: the structure of the eddy field is shaped by its interaction with the mean flow, and the eddy fluxes in turn modify the mean flow to complete the two-way wave-mean coupling.

The mean-field dynamics has considerable conceptual and practical advantages over the full nonlinear equations of motion. As result of our approximation, the eddy equations of motion (50,51) become linear in eddy quantities. We write the eddy PV fields as Fourier series in zonal wavenumber components $k_n = 2\pi n/L$

$$q_1(x,y,t) = \mathrm{Re}\left[\sum_{n=1}^{\infty} \tilde{q}_{1,n}(y,t) e^{ik_n x} \right] \qquad q_2(x,y,t) = \mathrm{Re}\left[\sum_{n=1}^{\infty} \tilde{q}_{2,n}(y,t) e^{ik_n x} \right]. \tag{54}$$

Equations (50,51) then imply that each wavenumber component n evolves independently of the others, interacting only through their mutual interaction with the mean flow. This is in contrast to the full nonlinear equations in which Fourier components interact directly. Since wavenumbers do not interact directly in the mean-field dynamics, it is mathematically consistent to retain a single zonal wavenumber k in the expansions (54) and write

$$q_1(x,y,t) = \mathrm{Re}\left[\tilde{q}_1(y,t) e^{ikx} \right] \qquad q_2(x,y,t) = \mathrm{Re}\left[\tilde{q}_2(y,t) e^{ikx} \right]. \tag{55}$$

The resulting equations of motion for the single wave and the mean flow are

$$\partial_t \tilde{q}_1 = \left[-ikU_1 - r + \kappa(\partial_{yy} - k^2)\right]\tilde{q}_1 + \left[-ik\partial_y Q_1\right]\tilde{\psi}_1 \quad (56)$$

$$\partial_t \tilde{q}_2 = \left[-ikU_2 - r + \kappa(\partial_{yy} - k^2)\right]\tilde{q}_2 + \left[-ik\partial_y Q_2 - dF_2(\partial_{yy} - k^2)\right]\tilde{\psi}_2 \quad (57)$$

$$\partial_t Q_1 = (k/2)\partial_y \mathrm{Im}\left(\tilde{\psi}_1 \tilde{q}_1^\star\right) - rQ_1 - \frac{1}{\rho_1 H_1}\partial_y \tau + \kappa \partial_{yy} Q_1 \quad (58)$$

$$\partial_t Q_2 = (k/2)\partial_y \mathrm{Im}\left(\tilde{\psi}_2 \tilde{q}_2^\star\right) - rQ_2 + dF_2 \partial_y U_2 + \kappa \partial_{yy} Q_2 \quad (59)$$

in which we have used the relation $\overline{v_i' q_i'} = -(k/2)\mathrm{Im}(\tilde{\psi}_i \tilde{q}_i^\star)$ to write the eddy PV fluxes explicitly in terms of the Fourier coefficient. Stars indicate complex conjugation. In equations (56)-(59), the retained wavenumber k is a free parameter. We choose k based on the dominant wavenumber observed in nonlinear model integrations. The mean-field dynamics is also often referred to as the quasilinear approximation. Based on this nomenclature, we will refer to the closed dynamical system (56)-(59) as the quasilinear model, abbreviated "QL". To mirror our naming convention we refer to the fully nonlinear dynamics (13)-(14) by the abbreviation "NL". We emphasize that the difference between NL and QL is in the EENL terms only. As these terms play no role in the zonally-symmetric fixed point solution, the QL dynamics has the same fixed point and stability properties as NL, with the exception of the influence of PV diffusion which is included in QL but not in NL.

In the full nonlinear dynamics (13,14), a flow initialized with energy concentrated in single zonal wavenumber component would nonlinearly produce a full spectrum of waves through the EENL terms. In the mean-field dynamics this scattering of energy to other waves does not occur and the interaction of a single wave with the mean flow can be consistently investigated. The choice to retain a single wavenumber constitutes an extreme simplification of the dynamics, reducing the dynamical variables of the model from two-dimensional fields fluctuating in time $\psi'(x, y, t)$ to one-dimensional Fourier structures varying in time $\tilde{\psi}_k(y, t)$. In addition to practical simplification, the mean field equations also provide conceptual clarity by isolating the effects of wave-mean flow sector of the model physics from the EENL effects. This separation allows us to evaluate the importance of EENL processes in determining the model's response to forcing. In the remainder of this paper we will compare solutions of the nonlinear and mean-field equations to evaluate the extent to which the mean-field theory can reproduce the response of the nonlinear model to changes in wind forcing. The success or failure of the mean-field dynamics in mirroring the behavior of the full model has important implications for our understanding of how eddies influence the mean climate state.

2.6 Numerical Implementation

The NL equations (13)-(14) are integrated numerically on a staggered finite-difference grid with $nx = 128$ points in the zonal direction and $ny = 64$ points in the meridional direction. This corresponds to a model grid spacing of $dx = dy \approx 15$ km, so that we have several grid points within each Rossby radius $R_d \approx 40$ km. PV inversion is performed spectrally. Advection terms are calculated in flux form and a van Leer flux limiter is used for numerical stability. We use a second-order Runge-Kutta method for the marching scheme with a time step of $dt = 1/64$ days. The model is initialized near the fixed point solution for low values of

the wind stress. For large values of wind stress $U_{1,FP}$ is so large that initialization near the fixed point constrains the timestep due to the CFL condition, so we instead initialize with zonal mean fields equal to those of the fixed point but rescaled by a coefficient with value less than one. Small scale noise is added to break the symmetry and allow the instability to develop. Model integrations are typically carried out for 5000 days, which was found to be sufficient to obtain reasonable flow statistics. For some parameter values very long runs (50000 days) were carried out, and the statistics were not found to change very much compared to the shorter integrations. The sensitivity of the model results to the spatial resolution was also tested. Model integrations at doubled resolution (Fig. 12, Appendix) showed minor quantitative differences when compared with the default resolution, but the similarity of the two solutions demonstrates that the model dynamics are sufficiently well-resolved at 64×128 resolution.

The QL equations (56)-(59) are solved numerically using finite-differences on an $ny = 64$ point meridional grid. PV inversions were performed using finite differences. The same marching scheme, time step, and initialization procedure was used as in NL. As the QL model is inexpensive to numerically integrate (even compared with our highly simplified two-layer QG model) we integrate the QL model for 100000 days to obtain reliable statistics. In many cases the QL model exhibits long transient oscillations after the initial instability, but these were eliminated from the statistics by averaging only over the second half of the model integrations.

3 Results

3.1 Reference Case

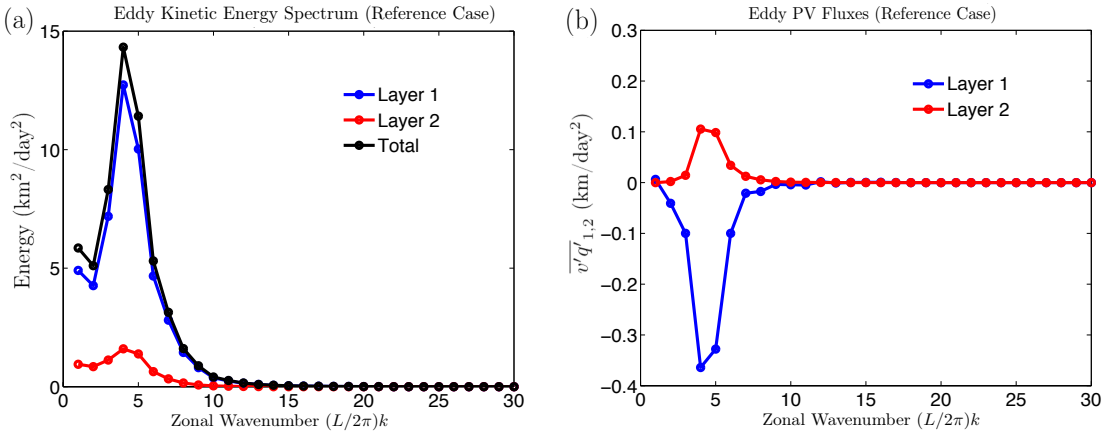

Figure 3: (a) EKE as a function of zonal wavenumber in the NL model (b) Eddy PV flux as a function of wavenumber in the NL model. Both EKE and PV flux show large peaks at zonal wavenumbers 4 and 5, indicating that these waves are dominant in the statistical mean state

We now compare the results of the NL and QL model integrations for the reference case $A = 1$ km/day^2, $r = 1 \times 10^{-4}$ day^{-1}, $d = 500$ km^2/day. Figure 3 (a) shows the time and

domain average EKE as a function of zonal wavenumber in the equilibrated NL state, where EKE is calculated as

$$EKE = \frac{H_1\langle u_1'^2 + v_1'^2\rangle + H_2\langle u_2'^2 + v_2'^2\rangle}{H_1 + H_2} = \frac{F_2\langle u_1'^2 + v_1'^2\rangle + F_1\langle u_2'^2 + v_2'^2\rangle}{F_1 + F_2}. \tag{60}$$

Angle brackets indicate a time and domain average. The contribution from each wavenumber was determined by expanding the velocity field in a Fourier series as in (54) and calculating the energy of each wavenumber component separately. The energy spectrum shows a clear peak at zonal wavenumber 4, with some energy at the neighboring wavenumbers and very little energy at small scales. Figure 3 (b) shows the time and domain mean eddy PV flux $\langle v'q'\rangle$ for the upper and lower layers as a function of wavenumber. In the upper layer the eddies flux PV poleward, decelerating the upper layer flow by (16). The eddy flux in the lower layer is in the opposite direction, with the eddies acting to drive the lower layer flow against bottom friction. The eddy flux spectrum indicates that zonal wavenumber 4 dominates the flux of PV, in addition to containing the most kinetic energy. Based on these observations, we take $k = 4$ as our QL wavenumber.

Figure 4 (a) and (c) show snapshots of the upper layer PV fields in QL and NL in statistical equilibrium. The zonal wavenumber 4 and 5 structures appearing in the energy spectrum are also visibly evident in the NL PV field. The NL and QL PV fields are qualitatively similar, although EENL effects in the NL model produce PV filaments that are not present in the QL model. The QL PV field is by design characterized by an exact wave-4 structure, since only $k = 4$ is included in our calculation.

Panels (b) and (d) in Fig. 4 show the zonal mean flow in the upper and lower layers for the QL and NL models. It is informative to compare these equilibrated turbulent structures to the fixed point solutions (35,36). For the reference parameter values, the upper and lower layer unstable fixed point jets have strengths $U_{1,FP} \sim 180$ km/day and $U_{2,FP} \sim 3$ km/day so that the fixed point baroclinic shear is $\mathcal{O}(175$ km/day). The shear maintained by the equilibrated turbulence is $\mathcal{O}(15$ km/day) at the channel center, indicating that the action of baroclinic eddies produces a dramatic barotropization of the flow. The magnitude of the upper layer flow is approximately 20 km/day ≈ 23 cm/s, which is realistic for the ACC.

The strengths of the zonal jets U_1 and U_2 are similar in the QL and NL models. Inspection of the upper layer flow in NL shows that the eddies have modified the meridional profile of the zonal jet in addition to severely reducing its strength relative to the fixed point solution. The initially sinusoidal profile has been intensified at the channel center and weakened in the flanks of the center jet, with the appearance of an additional slight inflections of the jet profile near $y = 200$ km and $y = 800$ km. The QL upper layer jet has a meridional structure qualitatively different from that of the NL jet. The QL jet is intensified at the channel center and weakened on the flanks in agreement with the NL profile. However, additional flank jets are evident in the QL simulation near the locations of the minor inflections seen in the NL profile. These strong flank jets do not seem to form in the NL system. As the upper-level QL jet is stronger than the NL jet in some regions of the channel and weaker in other regions, the QL dynamics may track the behavior of NL more closely in the domain-average picture in which these differences in structure may be partially averaged out. The lower layer jets of NL and QL agree much more closely than the upper layer jets, although the QL dynamics still produces additional meridional structure on the flanks of the sharpened center jet. Additional work is in progress to identify

the physical explanation for these differences in structure, which we suspect are due to the development within the jet of critical layers for the equilibrated wave which are smoothed out by the turbulence of the NL model.

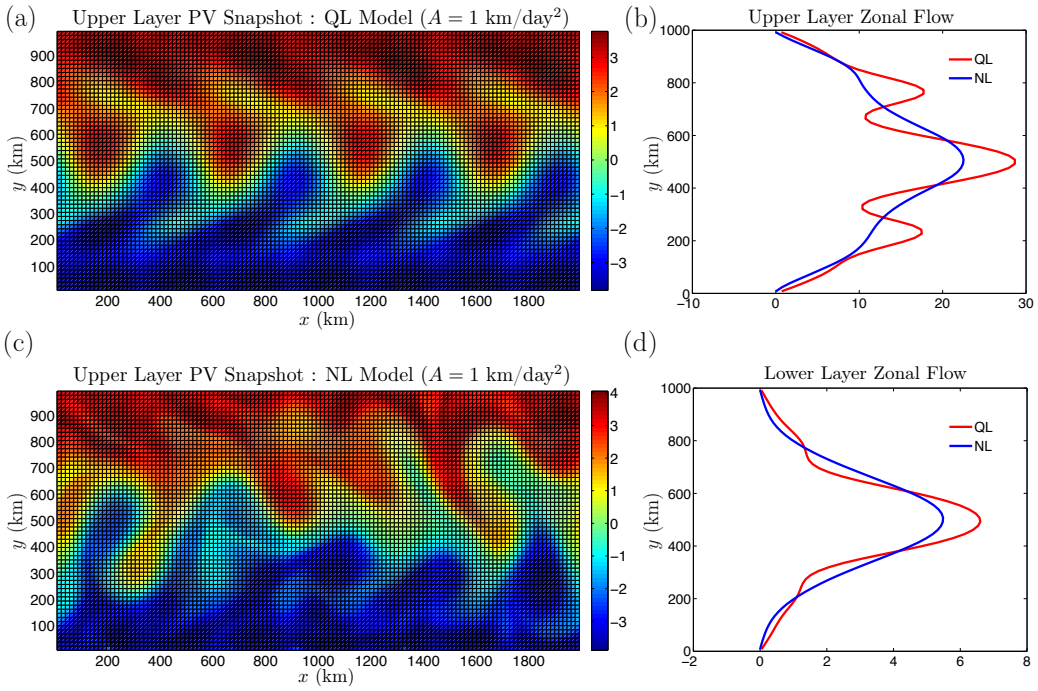

Figure 4: (a) Snapshot of upper layer PV in the QL model. (b) Upper level zonal mean flow in the QL (red) and NL (blue) models. (c) Snapshot of upper layer PV in the NL model. (d) Lower level zonal mean flow in the QL (red) and NL (blue) models. PV snapshots show qualitatively similar structures in both models, with NL showing a mixture of waves 4 and 5 as well as some small scale structure absent from the QL model. Zonal mean flows in QL and NL are close in amplitude but differ in meridional structure, with the QL dynamics producing a multiple jet structure that is not found in NL.

3.2 Model Response to Increasing Wind Stress

Motivated by the qualitative agreement between the QL and NL models in the reference configuration, we next vary the strength of the wind stress and compare the responses of NL and QL over a wide range of parameter space. Figure 5 shows the domain and time mean shear $U_1 - U_2$ as a function of the wind stress A for the NL and QL models. The abrupt change in the behavior of the QL curve at very weak wind stress is due to the onset of baroclinic instability, which sets in near $A = 0.25$ km/day in QL. The NL model is unstable for all plotted A values due to the absence of diffusion in NL system. Away from the instability boundary the shapes of the NL and QL curves are quite similar, with the behavior appearing to be loosely separated into two regimes. For relatively weak wind stress $A \lesssim 1$ km/day, the shear increases rapidly as A is increased. We emphasize that even in this relatively weak forcing regime the shear of the equilibrated state is much weaker than

that of the fixed point solution, and that the rate of increase of the shear with A is also much shallower than that which would result from the fixed point solution. The sharp increase of shear with A for the fixed point solution can be seen in the first few points of the QL curve before the flow becomes unstable. As A is increased beyond $A \approx 1$ km/day, the shear becomes less sensitive to changes in wind stress, indicating a degree of eddy saturation that occurs in both the QL and NL models. From Fig. 5 it does not appear that the shear ever becomes independent of A, which would correspond to complete eddy saturation, but we have not carried out model runs beyond $A = 7$ km/day.

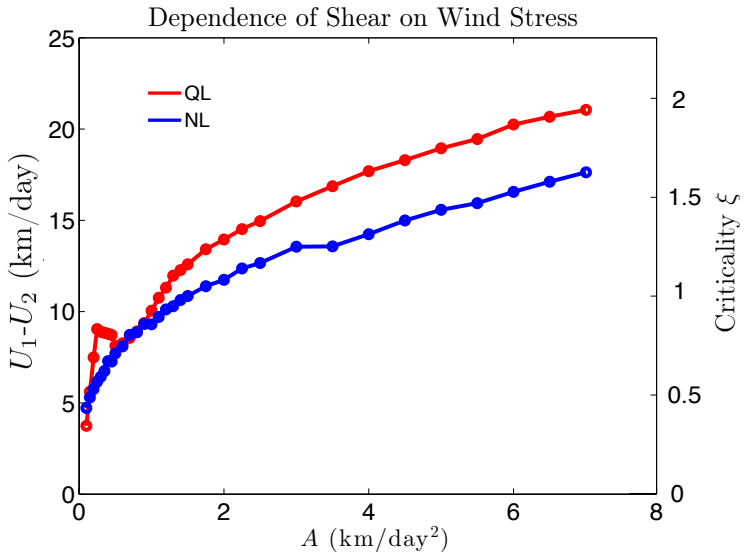

Figure 5: Domain and time average shear in statistical equilibrium in the QL (red) and NL (blue) models as functions of wind stress. Behavior in both models is characterized by increased sensitivity to wind stress at low values of A, transitioning to partial eddy saturation as the winds become stronger.

We also show the dependence of the criticality parameter ξ on wind stress in Fig. 5 (right axis). The criticality is defined as

$$\xi = \frac{f_0 s}{H_2 \beta} = \frac{F_2}{\beta}(U_1 - U_2) \tag{61}$$

and serves as a nondimensionalization of the shear. A commonly-invoked theoretical argument [18] suggests that baroclinic turbulence will adjust the mean state such that the lower layer PV gradient vanishes. This is motivated by the necessary condition for baroclinic instability that the PV gradient change sign somewhere in the domain: as the upper layer PV gradient is positive, zero PV gradient in the lower layer is the marginal state to which the eddies relax the mean state. Ignoring relative vorticity, the lower layer PV gradient is

$$\partial_y Q_2 = \beta - F_2(U_1 - U_2) \tag{62}$$

so that a vanishing gradient implies that $F_2(U_1 - U_2)/\beta = \xi = 1$. Values of the criticality $\xi > 1$ then correspond to interfacial slopes steeper than those expected from the marginal

instability criterion and a more strongly reversed lower layer PV gradient. Criticality values $\xi < 1$ indicate the opposite mean state properties. The model results shown in Fig. 5 indicate that $\xi = 1$ does not appear to be a preferred value for this system. In the NL dynamics, the turbulent state is subcritical for weak wind stress and passes through $\xi = 1$ to become supercritical for larger wind stress. The QL model shows similar behavior, although the subcritical range is obscured by the transition to baroclinic instability. These results are consistent with the recent idealized modeling study of Jansen and Ferrari [6], who showed that the turbulent state of the atmosphere can be moved from a subcritical to a supercritical regime by varying the external control parameters.

As we are interested in the role of the eddies in determining the equilibrated turbulent state, we next relate the mean states shown in Fig. 5 to the properties of the eddy field. Figure 6 (a) shows the eddy diffusivity K in the NL and QL models as a function of wind stress. Both models produce eddy diffusivities on the order of $\mathcal{O}(100 \text{ km}^2/\text{day}) \approx 1000 \text{ m}^2/\text{s}$, which is in the realistic range for the ocean at mid depths [10]. We estimate K using two independent methods. First, taking the interfacial slope s from our numerical simulations we can solve for K in (28) to obtain

$$K_{\text{theory}} = \frac{\tau}{f_0 \rho_1 s} = \frac{\tau/(\rho_1 H_1)}{F_1(U_1 - U_2)}. \tag{63}$$

We use the subscript 'theory' to indicate that this estimate of K is not based on observations of the PV flux and gradient from the numerical model, but is derived from the equilibrium state using the assumptions outlined in Section 2.2. We also estimate K directly from our numerical simulations using the definition

$$K_{\text{est}} = -\frac{\overline{v_1' q_1'}}{\partial_y Q_1} \tag{64}$$

which we calculate at every model timestep and average over the domain and in time to estimate K. Figure 6 (a) shows that the eddy diffusivity depends strongly on the wind stress in both the QL and NL dynamics, increasing by a factor of 4 as A is varied from 1 km/day^2 to 7 km/day^2. The diffusivity becomes somewhat less sensitive to A as A is increased. The QL model equilibrates with a larger shear than the NL model in Fig. 5, and correspondingly the QL eddy diffusivity is weaker than that of the NL model.

Mixing length arguments suggest that K is related to the EKE through a functional relationship of the form $K \sim \sqrt{EKE}$ [2]. Figure 6 (b) shows the domain-average total EKE as a function of wind stress in NL and QL, calculated using equation (60). The EKE behaves similarly in the two models as A is increased. For very small A values the QL EKE is exactly zero since the fixed point is stable. Beyond the instability threshold the EKE of both NL and QL increase close to linearly as wind stress is increased, with the QL EKE growing more rapidly with A than the NL EKE. For $A \lesssim 2$ km/day^2, the NL EKE exceeds the QL EKE as the NL model is further from the threshold for baroclinic instability. For larger values of the wind stress the eddies in the QL model contain more energy than those in the NL model in spite of the additional diffusion in the QL dynamics. This suggests that the EENL terms produce an effective eddy viscosity acting on the eddies themselves, scattering energy from the wavenumbers capable of extracting energy from the mean state to

small-scale damped waves where the energy is dissipated. In our numerical implementation of NL this small-scale damping may be accomplished by the flux limiter or by numerical diffusion. Although we do not quantitatively examine the scaling relationship between K and EKE in this work, the downward concavity of the diffusivity curve and approximate linearity of the EKE with A is suggests that a relationship similar to $K \sim \sqrt{EKE}$ may be applicable to our results. However, it appears that if such a functional relationship is valid it may not hold across both models, as for larger A values the QL EKE is greater than the NL EKE, while the diffusivity of the NL dynamics is always larger than that of the QL dynamics.

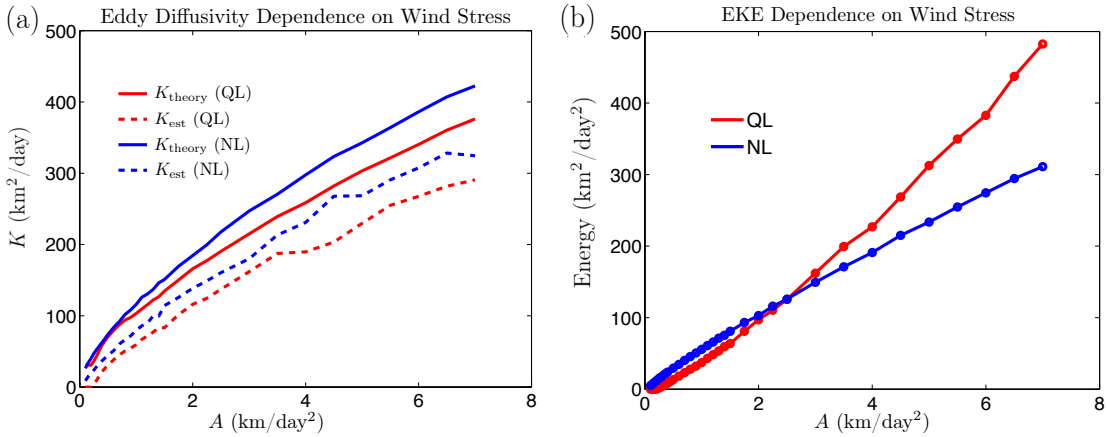

Figure 6: (a) Eddy diffusivity K in the QL (red) and NL (blue) models as functions of wind stress. K_{theory} is an estimate based on the equilibrium shear using equation (63), while K_{est} is an estimate based directly on the eddy flux and PV gradient in model simulations using equation (64). The results show that K increases substantially with increasing winds. (b) EKE as a function of wind stress in the QL (red) and NL (blue) models. In both models EKE increases approximately linearly with A.

3.3 Parameter Sensitivity

In Section 3.2 we presented the behavior of the NL model as the wind stress was increased and evaluated the ability of the mean-field dynamics to reproduce the observed NL behavior. In this section we vary the drag parameters d and r to test the robustness of the general agreement between the QL and NL models demonstrated in the previous section. Figure 7 shows the time and domain mean shear as a function of wind stress in the NL and QL models for four additional parameter cases. In panels (a) and (b) the bottom drag coefficient d is halved and doubled, respectively, relative to its reference value of $d = 500$ km^2/day. In panels (c) and (d) the Rayleigh drag coefficient r is halved and doubled with respect to its reference value of $r = 10^{-4}$ day^{-1}. For each case, all parameters are held constant except A and the drag parameter that was changed for that sensitivity test. In all cases the qualitative behavior of the NL model as A is increased is the same as discussed for the reference case. For weak wind stress the shear increases rapidly with A, with the sensitivity of the shear to the wind stress lessening as A is increased. For large wind stress the shear

appears to increase approximately linearly with A. It is clear from Fig. 7 that the success of the QL model in reproducing the NL shear scaling is robust to alternate choices of the the drag parameters.

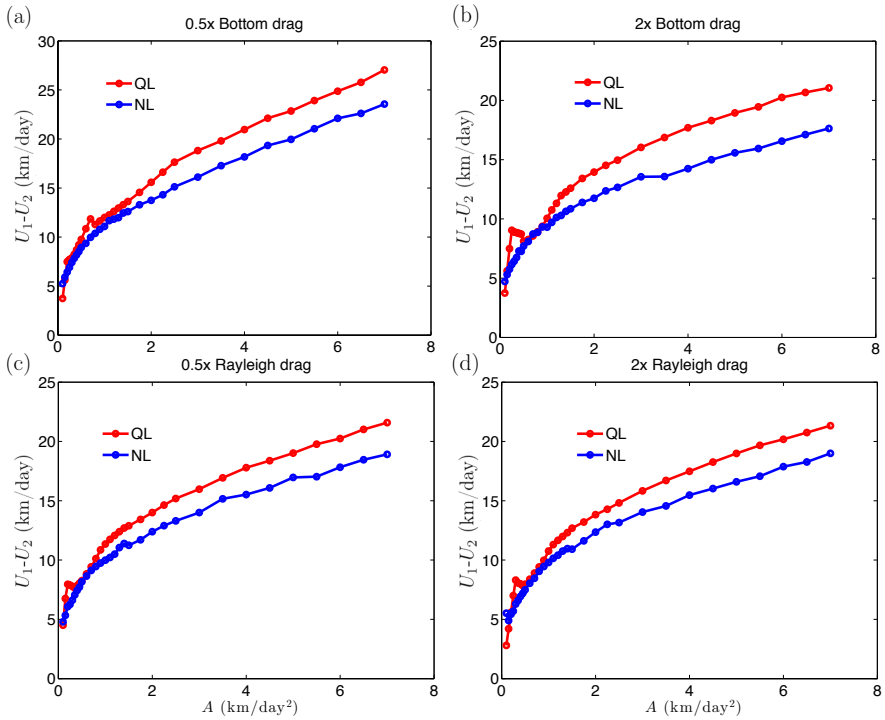

Figure 7: Testing the robustness of the agreement of QL and NL to changes in the drag parameters. All panels show the time and domain average shear in the QL (red) and NL (blue) models as functions of wind stress, for four different parameter cases. (a) $d = 250$ km^2/day, $r = 10^{-4}$ s^{-1}. (b) $d = 1000$ km^2/day, $r = 10^{-4}$ s^{-1}. (c) $d = 500$ km^2/day, $r = 0.5 \times 10^{-4}$ s^{-1}. (d) $d = 500$ km^2/day, $r = 2 \times 10^{-4}$ s^{-1}. The model behavior is similar in all cases.

Comparison of the NL curves in Fig. 7 (a) and (b) shows that the equilibrium shear in NL weakens as the bottom drag is increased for fixed A (note the difference in scale between (a) and (b)). This result is shown more clearly in Fig. 8 (b), which shows the equilibrium shear in QL and NL for the reference wind stress value $A = 1$ km/day^2 and three values of the bottom drag, corresponding to our reference drag $d = 500$ km^2/day and the halving and doubling cases shown in Fig. 7 (a) and (b). Both QL and NL show weakening shear with increasing bottom drag. Based on the scaling relation (28), this indicates that the eddy diffusivity K increases as the bottom drag is increased for constant winds. The physical explanation for this behavior is not obvious. From (29) increasing bottom drag results in a reduced lower level flow. However, this effect only changes the barotropic component of the flow, whereas the shear component is the one most relevant to the eddy physics. The shear associated with the fixed point solutions (35) and (36) also does not depend on d, in the limit $dF_2/r \gg 1$ relevant to this work. Understanding the physical mechanisms behind the parameter dependencies shown in Fig. 8 is an important future direction of the work.

The equilibrated shear also depends to some extent on the bulk Rayleigh drag as shown in Figs. 7 (c), (d) and 8 (a). As r is increased at constant wind, the shear decreases slightly in NL and somewhat more substantially in QL. The relation (28) implies that this decrease in shear results from an increase in the eddy diffusivity with increasing Rayleigh drag. This is somewhat surprising since the drag acts to remove energy from the eddy field, thus presumably weakening the eddy fluxes. However, the arguments in Section 2.2 were based on the assumption that the diabatic effects could be ignored in the mean budgets. In the complete dynamics, the drag r acts not only on the eddies but on the mean state as well, including directly damping the interface deflection through (18). The decrease in shear with increasing drag in Fig. 8 (a) likely results from a competition between the direct diabatic damping of the shear and the simultaneous reduction of the EKE and corresponding eddy diffusivity by the drag.

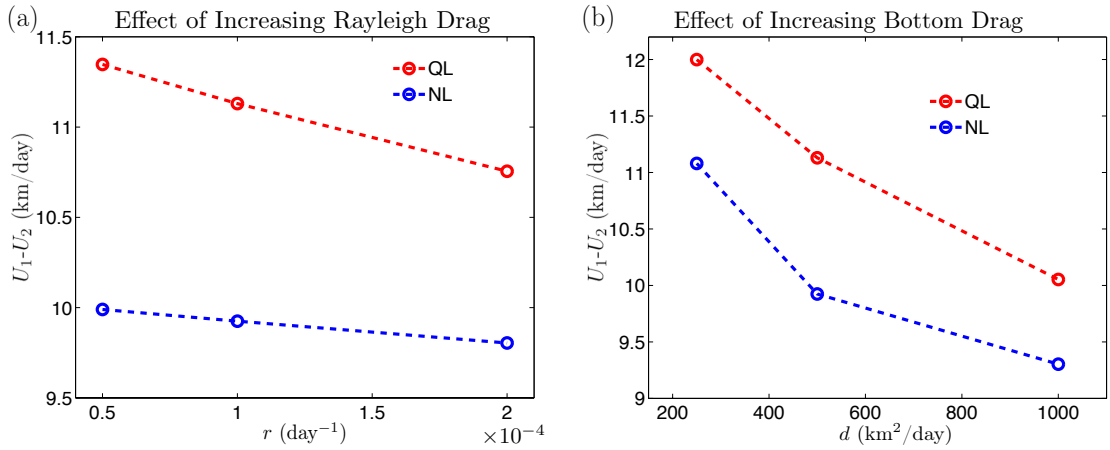

Figure 8: (a) Time and domain average shear in the QL (red) and NL (blue) models as functions of Rayleigh drag r. Wind stress is fixed at $A = 1$ km/day^2. (b) Same, but for varying bottom drag d. The equilibrium shear is seen to weaken with both forms of drag in both the QL and NL models.

In Fig. 9 we show the meridional structure of the shear for the reference wind stress $A = 1$ km/day^2 and the four alternate drag parameter choices previously discussed. As was found in the reference case (Fig. 4), important qualitative differences between the shear profiles of NL and QL are visible. The QL model forms multiple jets in all cases. Similar flank jets are also found in the NL model in the case of weak bottom drag (Panel (a)), but the additional jets are much weaker than their QL counterparts. Evidently, the wave-mean flow dynamics of a single zonal Fourier component has a strong tendency to produce multiple jets that is strongly suppressed in the NL dynamics. In the next section we will show the results of a preliminary attempt to produce a more realistic jet structure in the QL model by including additional zonal wavenumber components and modeling the effect of EENL interactions with stochastic forcing.

Based on our observations of the NL EKE and PV flux spectra in Fig. 3, we chose $k = 4$ as our single zonal wavenumber component in the QL dynamics. Figure 10 (a) shows the shear as a function of wind stress for reference drag values in the QL dynamics and in

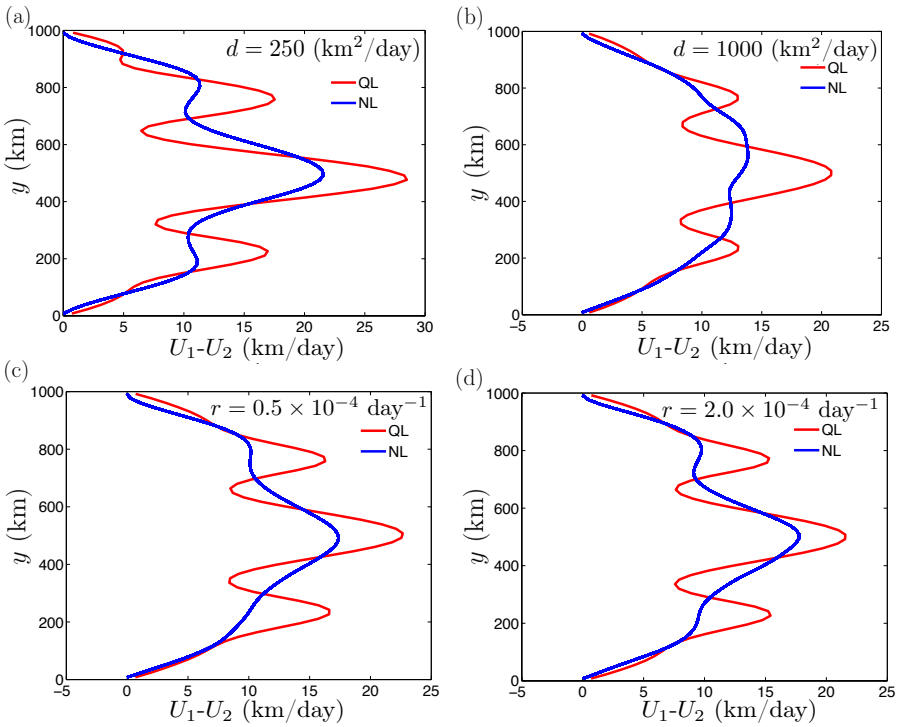

Figure 9: Comparison of the QL and NL profiles of time and zonal mean shear for different drag values. In all cases QL produces multiple jets that are not seen in NL. (a) $d = 250$ km^2/day, $r = 10^{-4}$ s^{-1}. (b) $d = 1000$ km^2/day, $r = 10^{-4}$ s^{-1}. (c) $d = 500$ km^2/day, $r = 0.5 \times 10^{-4}$ s^{-1}. (d) $d = 500$ km^2/day, $r = 2 \times 10^{-4}$ s^{-1}.

two alternate QL models in which $k = 3$ and $k = 5$ were chosen as the QL wavenumbers. Although the choice of wavenumber does have a quantitative effect on the shear, the shapes of the curves are quite similar for all three wavenumber choices. The $k = 3$ model maintains the largest shear, indicating that the eddy diffusivity is smallest for this choice of k. This is conceptually consistent with our observations of the NL spectrum, which showed that the EKE and PV flux associated with $k = 4$ and $k = 5$ were comparable while $k = 3$ was relatively weak. We take this as an indication that the $k = 3$ wave is less efficient at extracting energy from the equilibrated NL mean state than $k = 4$ and $k = 5$, consistent with the behavior shown in Fig. 10 (a) for the QL models.

Although we have chosen to work with the maximally-simplified QL dynamics in which only a single wavenumber is retained, it is also possible to formulate the QL dynamics with more than one wavenumber. In such a model each eddy component $\tilde{q}_{1,k}(y,t)$ has its own evolution equation of the form (56), (57). Each component interacts with the same mean field $Q_1(y,t)$, $Q_2(y,t)$, so that the waves are indirectly coupled through their mutual interactions with the mean flow. Figure 10 (b) shows an example of the results of a QL integration in which the first 8 wavenumber components $k \in (2\pi/L)\{1,\ldots,8\}$ were retained and reference parameter values were chosen. During the initial transient phase of instability growth, all unstable waves begin to grow. (See Fig. 2 (b) for the instability growth rates as a function of k for this case). Waves 3,4, and 5 grow to large amplitude, while all

other waves remain too weak to be seen on our axis scale. At equilibrium waves 4 and 5 persist. The structure of the resulting jets (not shown) is similar to the jets produced by the $k = 4$ single-wave model. In particular, the multi-wave QL dynamics continues to produce multiple jets in qualitative disagreement with NL solutions.

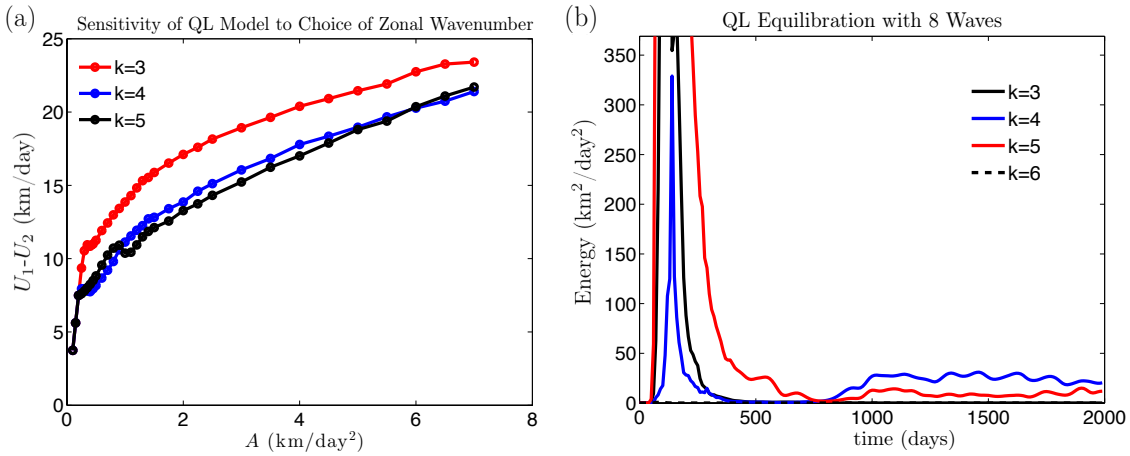

Figure 10: (a) Time and domain average shear as a function of wind stress for QL models in which different zonal wavenumbers were retained. All three cases show similar qualitative behavior, but the $k = 3$ QL model supports a larger equilibrium shear. (b) Time series of EKE for each wavenumber in a QL model run for reference parameter values in which the first 8 wavenumber components were retained. Initially all unstable waves grow, and some waves reach large amplitude before decaying to zero asymptotically. Two waves, $k = 4$ and $k = 5$, survive at finite amplitude in the statistical equilibrium state.

3.4 Stochastically-Driven QL Dynamics

In this section we present the results of a preliminary attempt to resolve the discrepancy between the jet structures of the QL and NL dynamics. Our approach is to introduce additional stochastic forcing into the QL model with multiple wavenumber components. The motivation for this model comes from several observations. First, it is clear from the NL energy spectrum (Fig. 3) that although the EKE is concentrated at $k = 4$ and $k = 5$ in the reference simulation, the wavenumber spectrum is populated up to about wave 10, with most of these waves producing non-negligible contributions to the PV flux. Second, the timeseries in Fig. 10 (b) shows that wavenumbers that are not present in the statistical equilibrium state still have the capacity to extract substantial energy from the mean flow as demonstrated by their rapid growth at early times. Although the equilibrium state has been adjusted so that waves other than $k = 4$ and $k = 5$ have negative growth rates on the mean state, the linear dynamics of these waves remains highly non-normal and thus can exhibit large transient growth if they are somehow excited. In the QL dynamics no such excitation occurs and these waves remain at zero amplitude forever. This is an unrealistic aspect of the QL model, since EENL interactions in the NL dynamics scatter energy into all wavenumbers. We make the simplifying assumptions that the EENL scattering is not

correlated in time and not dependent on the system state, and model the effect of the EENL terms by adding stochastic forcing to the evolution equations for all wavenumber components in the QL dynamics.

The stochastic QL model modifies the usual QL equations of motion to include an additional term on the RHS of the eddy PV equations:

$$\partial_t \tilde{q}_{1,k} = \left[-ikU_1 - r + \kappa(\partial_{yy} - k^2)\right] \tilde{q}_{1,k} + \left[-ik\partial_y Q_1\right] \tilde{\psi}_{1,k} + \varepsilon G_k(y,t) \tag{65}$$

$$\partial_t \tilde{q}_{2,k} = \left[-ikU_2 - r + \kappa(\partial_{yy} - k^2)\right] \tilde{q}_{2,k} + \left[-ik\partial_y Q_2 - dF_2(\partial_{yy} - k^2)\right] \tilde{\psi}_{2,k} + \varepsilon G_k(y,t). \tag{66}$$

The evolution equations for Q_1 and Q_2 remain the same, since EENL terms appear only in the eddy equations in the NL dynamics. In these equations $G_k(y,t)$ is a random forcing term that is applied equally in both layers for simplicity. We choose our random forcing to be δ-correlated in time and correlated in space with a structure $g_k(y,y')$ such that $\langle G_k(y,t) G_k^\star(y',t')\rangle = g_k(y,y')\delta(t-t')$ where angle brackets indicate the ensemble mean over realizations of the noise. We take the stochastic forcing to be equal for all wavenumbers so that $g_k(y,y') = g(y,y')$. We choose the spatial correlation structure of the noise to be given by

$$g(y,y') = \exp\left(-\frac{(y-y')^2}{\ell_c^2}\right) \exp\left(-\frac{(y-\frac{W}{2})^2}{2\Delta^2}\right) \exp\left(-\frac{(y'-\frac{W}{2})^2}{2\Delta^2}\right). \tag{67}$$

This correlation function produces noise with Gaussian correlation in space with correlation length ℓ_c and noise amplitude peaked in the channel center. We take $\ell_c = 78$ km and $\Delta = 156$ km. These choices ensure that the noise is locally smooth over a few model gridpoints and that the amplitude of the forcing is substantial over the middle third of the channel, tapering toward the boundaries. This choice of forcing structure was chosen for its simplicity. An important extension of this work will be to use observations of EENL scattering in the NL dynamics to understand what forcing structure is most realistic of the true EENL dynamics. The parameter ε controls the overall amplitude of the noise forcing and has units of day$^{-3/2}$ so that ε^2 has units of potential enstrophy injection rate. In the NL model the EENL interactions do not inject energy into the eddy field, but rather move energy from wavenumber to wavenumber while leaving the total EKE invariant. Our stochastic forcing is deficient in this sense because forcing of the form described above injects energy directly into the eddy field. The stochastic parameterization could thus be improved by augmenting the eddy dissipation such that the eddy energetics are consistent with those of NL [5]. For simplicity we ignore these concerns and proceed with the formulation described above as a first step. We refer to the stochastic dynamics introduced above as the stochastic quasilinear model (SQL).

Figure 11 summarizes several results from SQL. All SQL integrations were performed with reference values for the wind stress and drag parameters, and the first six zonal wavenumber components were retained in the calculations. Panel (b) shows the time evolution of the energy of each wavenumber component during a 10000 day model integration with stochastic forcing strength $\varepsilon = .05$ day$^{-3/2}$. It is clear that all waves are excited and fluctuate at finite amplitude. Wavenumbers 4 and 5 (cyan and green curves) are no longer dominant, with the largest contribution to the eddy energy being due to $k = 1$. This is clearly seen in panel (c) which shows the time average EKE spectrum. The spectrum is red

and in poor agreement with the NL spectrum shown in Fig. 3. Note, however, that our maximally simple forcing in which each component of the eddy PV is forced with equal amplitude leads to a preferential injection of energy into the large scales (enstrophy is injected into each scale equally). This forcing bias, together with the action of diffusion to dissipate higher wavenumbers, may underlie the complete lack of agreement between the SQL and NL spectra. Panel (d) shows the dependence of the total EKE on the forcing strength. As expected, the eddies are more energetic when they are forced more strongly, and we expect this stronger eddy field to suppress the equilibrium shear.

The SQL equilibrium shear profiles are shown in Fig. 11 (a) for three values of the stochastic forcing amplitude, with the results of the NL reference case reproduced for comparison. For the smallest value of ε the shear profile is close to that of the ordinary QL model, showing strong jets on the flanks of the center jet. As ε is increased both the amplitude and the structure of the jets undergo substantial changes. The amplitude of the shear decreases as ε is increased, consistent with our understanding that the stochastic forcing supports the transient growth of waves whose eddy fluxes barotropize the zonal flow. The flank jets also weaken substantially as ε increases. For $\varepsilon = .05$ day$^{-3/2}$ (red curve), the jet structure is quite similar to that of the NL model. The amplitude of the shear, however, is too weak for this choice of forcing. Keeping the correlation structure of the forcing fixed and varying the parameter ε only, it is not possible to accurately fit the NL jet structure: either the strength or the structure of the shear can be approximately matched, but matching both simultaneously is not possible. However, the reduction of the strength of the unrealistic flank jets when stochastic forcing is included is an encouraging result, and future work with the SQL model will involve experimenting with the forcing structure $g_k(y, y')$ to evaluate whether SQL is capable of producing fully-realistic jet structures and amplitudes.

4 Discussion and Conclusion

The goal of this work is to advance our theoretical understanding of the interactions between eddies and the large scale mean state in baroclinically unstable flow driven by surface stress. In particular, we are interested in understanding how eddy-mean flow interactions change in response to changes in the external forcing. The ACC provides a concrete example system for which the external forcing is changing and the eddy response must be understood if we are to understand the response of the mean state. Theoretical models of the ACC mean state typically rely on the assumption of eddy diffusion. The manner in which the eddy diffusivity is parameterized in terms of the large-scale variables in such models can be the determining factor in the model predictions of the ACC response to changing forcing. Although the sensitivity of model predictions to the eddy diffusion parameterization indicates that the eddy diffusivity is a quantity crucial to our understanding of the turbulent dynamics, no accepted theory exists to predict its value or how it depends on the external parameters of the system. In this work, we make progress on this problem by demonstrating that a reduced dynamics, the mean-field equations, reproduces many aspects of an idealized, but fully turbulent, model of the ACC, including the variation of important mean state properties as the external forcing is varied. Although the theoretical prediction of mean state variations with forcing remains an open problem, the identification of the mean-field model as a significantly simplified theoretical framework that contains the essence of the

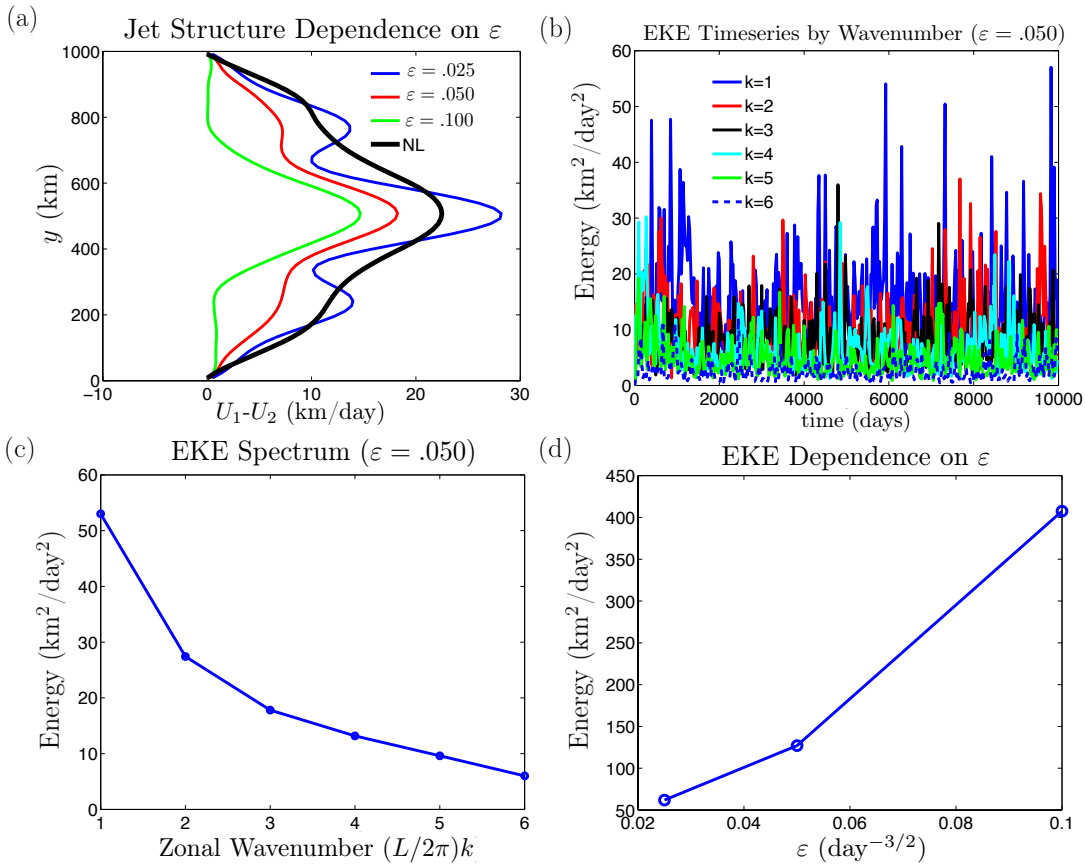

Figure 11: Summary of results of the stochastically-driven QL model. In all calculations reference parameter values were used and 6 zonal wavenumber components were retained. (a) Equilibrium shear profiles for three stochastic forcing strengths ε. The shear is seen to weaken overall as ε is increased, as well as shift toward a single-jet meridional structure. (b) Time series of EKE for each wavenumber in the stochastic model. All waves are sustained at finite energy in the equilibrium state. (c) Time average EKE spectrum for the stochastic model. In disagreement with the NL reference spectrum in Fig. 3, the eddy field is energetically dominated by the largest structures. (d) Total EKE as a function of stochastic forcing strength.

eddy-mean flow interaction and its dependence on the external model parameters provides a promising pathway for future efforts toward understanding the physics of the ACC response to forcing.

We used the idealized two-layer QG model in a flat-bottom channel configuration as our model ACC. We refer to this fully-nonlinear model formulation as the NL model. The flow was driven by wind stress at the surface, with the injected momentum being removed from the system in the lower layer by bottom friction. For very weak wind stress the flow is baroclinically stable, but the flow becomes unstable and turbulent for wind strengths that are realistic for the SO. By integrating the model equations numerically to a statistically-steady state for different values of the wind forcing, we assessed how the slope of the

interface, or equivalently the baroclinic component of the zonal mean flow, responded to changes in the winds. For weak winds the mean state was very sensitive to changes in forcing, with the shear increasing rapidly as the winds were increased. The shear responded less sensitively to further increases in the winds, demonstrating eddy saturation to some degree. However, the shear was not found to become entirely independent of the winds for any range of parameters tested, and so the model does not appear to exhibit complete eddy saturation.

We formulated the mean-field model by removing eddy-eddy advection terms from the equations of motion and retaining a single zonal wavenumber component in the eddy field. We refer to the mean-field equations by the abbreviation QL. In the domain mean picture, this highly simplified theoretical model reproduced many qualitative aspects of the NL dynamics. The dependence of the mean shear on the wind stress in QL mirrored that of NL, with differences occurring primarily at the quantitative level. The QL model also reproduced the sense of the dependence of the mean state on the imposed drag parameters. Our QL experiments demonstrated that the QL model robustly reproduces the domain-mean properties of the NL dynamics over a wide range of parameters in spite of the substantial simplifications made in deriving the model equations. Our results indicate that, in the domain mean sense, the strength and parameter-dependence of the eddy diffusivity are not fundamentally controlled by eddy-eddy processes.

We also compared the QL and NL models in the zonal mean, but not channel-mean, picture. When the channel-mean was not taken, important differences between the two models were evident. The equilibrated meridional structure of the shear flow in the NL takes the form of a broad single jet intensified at the channel center. In contrast, the QL equilibrium jet structure features multiple jets, with additional strong jets occurring on the flanks of the center jet. These qualitative differences in structure occur over all tested parameter ranges. This fundamental difference in structure points to qualitative differences in model physics that should be resolved if the QL dynamics is to be used to understand the NL model behavior.

In an attempt to improve the agreement between the meridional jet structures of the QL and NL model, we modified the QL dynamics to include additional wavenumber components and stochastic forcing as a parameterization of the EENL terms appearing in the NL dynamics. When stochastic forcing was included, the QL model attained an equilibrium state with a populated energy spectrum, and the flank jets were seen to weaken and disappear as the strength of the noise was increased. However, the energy spectrum of the stochastic model was in poor agreement with that of NL, and the QL jet amplitudes were too weak when compared with those of NL when the noise was strong enough to suppress the unrealistic multiple jets. We believe that these failures of the stochastic model may be due to bias introduced by the simplified structure chosen for the noise forcing as well as the diffusion introduced into the QL model for reasons of numerical stability.

The results presented here constitute a step toward understanding the relationship between the QL and NL dynamics but many aspects of the problem require additional research. At the level of the NL dynamics, a more detailed consideration of the eddy energy budget is required to understand the effects of the various forms of drag on the eddy field, and also how energy is passed between wavenumbers by eddy-eddy interactions. These results will be useful for informing the parameterization of the eddy-eddy terms in the QL dynamics.

Incorporating an improved noise parameterization is likely to improve the realism of the QL jet structure.

Beyond the problem of simply reproducing the NL simulation results with the QL model, it also remains an open problem to leverage the simplicity of the QL dynamics to develop a theoretical understanding of eddy-mean flow interactions in this problem. In the QL model without stochastic forcing, a possible approach is to identify and trace the unstable fixed point solution that exists, at least in some cases, beneath the fluctuating equilibrium state as a function of the wind stress. This fixed point consists of an equilibrated baroclinic wave and a steady mean flow, and becomes unstable in a supercritical Hopf bifurcation to an oscillatory state which becomes chaotic as the 'turbulent' QL state is reached. As the fluctuations in equilibrium appear to remain fairly close to this fixed point, the unstable fixed point solution is a relatively simple, time-independent mathematical object whose analysis may lead to a physical understanding of how eddy fluxes are determined in cooperation with the mean state. In the case of the stochastic QL model, a theoretical framework for analyzing the statistical mean equilibrium state has been developed by Farrell and Ioannou [4]. A promising future direction of this research is to use their covariance-matrix formalism to understand how the ensemble-mean eddy fluxes are determined by interaction with the mean state.

Our decision to model the ACC using the two-layer QG equations in a flat-bottomed reentrant channel was motivated by its simplicity. However, it is well-established that bottom topography plays an important role in the ACC dynamics. In a flat-bottom geometry the overall momentum balance must be between momentum injection by the winds and removal by bottom drag. This requires the development of a strong barotropic flow component capable of dissipating the required amount of momentum at the bottom. In the real ACC the momentum balance is between wind input and bottom form drag on topography, and the barotropic flow is weak. Flow over bottom topography also produces stationary waves that can have a significant effect on the ACC stratification by increasing the efficiency of eddy heat transport and correspondingly shallowing isopycnal slopes [1]. Our idealized model cannot account for these effects in its current formulation. However, topography could in principle be included in both the NL and QL models discussed in this work, and understanding the impact of topography in our framework is an important future direction.

5 Acknowledgments

I thank Glenn Flierl and Raf Ferrari for their help and guidance during my work on this project, and Brian Farrell for valuable comments on the manuscript. I also thank the organizers, participants, and Fellows of the 2014 WHOI GFD program for making the summer educational and enjoyable.

6 Appendix: Sensitivity of NL Model to Numerical Resolution

Figure 12 shows a comparison of nonlinear model runs at two different resolutions: the default resolution with 64×128 spatial grid points, and a doubled resolution run with

128×256 gridpoints. Reference parameter values are used for wind and drag. Panels (a) and (c) show snapshots of the upper layer PV fields. Panels (b) and (d) show the statistical mean upper and lower layer zonal jets. The PV fields show similar features and have similar characteristic magnitude in both cases. The higher resolution run shows some small-scale filamentation that is less prominent in the default resolution case. However, these small-scale features do not appear to dominate the flow. The time mean flow is also nearly identical in the two runs. The mean flow in the doubled-resolution run is not perfectly symmetric about the channel center. This is due to an insufficiently long period of averaging due to the increased computational cost to run the model at this resolution. Based on Fig. 12 we conclude that 64×128 gridpoints is sufficient to resolve the structures most important to the dynamics, at least in the parameter ranges considered here.

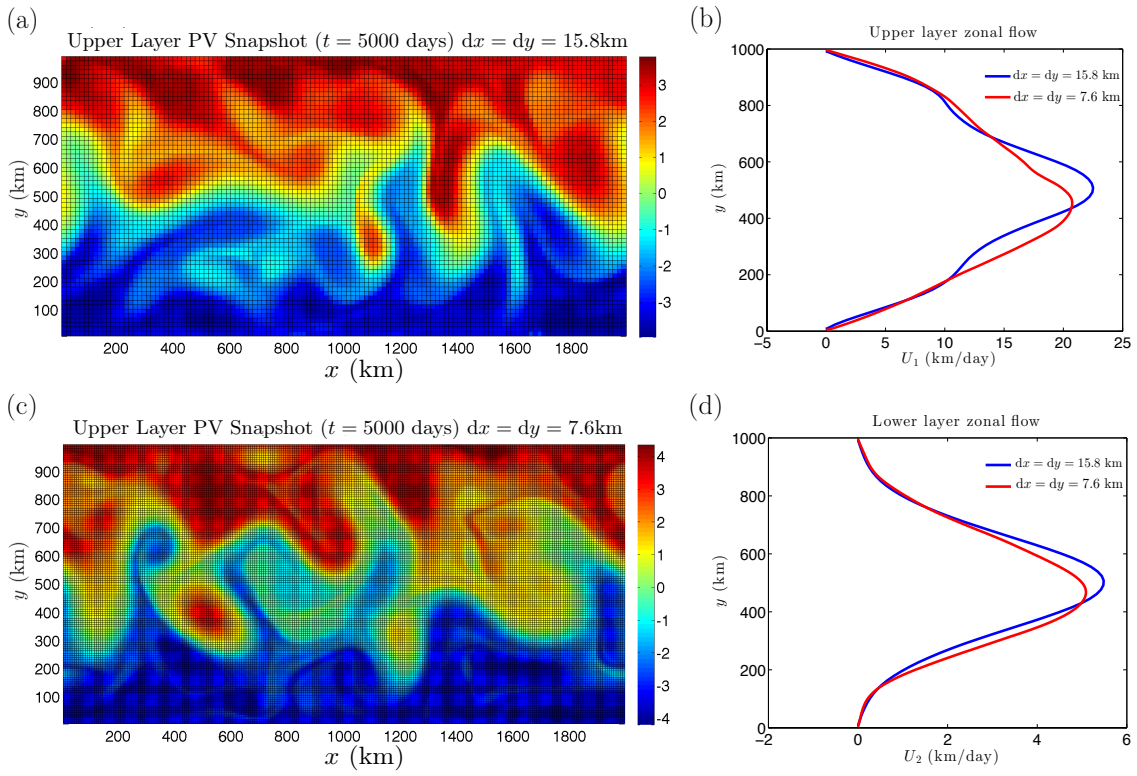

Figure 12: Test of spatial resolution in the NL model. Default resolution is 64×128 gridpoints, doubled resolution is 128×256 gridpoints. Panels (a) and (c) show snapshots of the upper layer PV fields. Although some smaller scale features are seen in the high resolution case that are absent from the default resolution case, the PV field still appears to be dominated by wave 4 and wave 5 structures. Panels (b) and (d) show the upper and lower level zonal mean flows in statistically steady state. High resolution jets (red) show some deviations from perfect cross-channel symmetry due to insufficiently long averaging periods. The high and default resolution flows are of nearly the same amplitude and similar meridional structure.

References

[1] R. Abernathey and P. Cessi, *Topographic Enhancement of Eddy Efficiency in Baroclinic Equilibration*, Journal of Physical Oceanography, 44 (2014), pp. 2107–2126.

[2] R. Abernathey, J. Marshall, and D. Ferreira, *The Dependence of Southern Ocean Meridional Overturning on Wind Stress*, Journal of Physical Oceanography, 41 (2011), pp. 2261–2278.

[3] C. W. Boening, A. Dispert, M. Visbeck, S. R. Rintoul, and F. U. Schwarzkopf, *The response of the Antarctic Circumpolar Current to recent climate change*, Nature Geoscience, 1 (2008), pp. 864–869.

[4] B. Farrell and P. Ioannou, *Structural stability of turbulent jets*, Journal of the Atmospheric Sciences, 60 (2003), pp. 2101–2118.

[5] B. F. Farrell and P. J. Ioannou, *A Theory of Baroclinic Turbulence*, Journal of the Atmospheric Sciences, 66 (2009), pp. 2444–2454.

[6] M. Jansen and R. Ferrari, *Macroturbulent Equilibration in a Thermally Forced Primitive Equation System*, Journal of the Atmospheric Sciences, 69 (2012), pp. 695–713.

[7] A. Kuo, R. Plumb, and J. Marshall, *Transformed Eulerian-mean theory. Part II: Potential vorticity homogenization and the equilibrium of a wind- and buoyancy-driven zonal flow*, Journal of Physical Oceanography, 35 (2005), pp. 175–187.

[8] C. Le Quere, C. Roedenbeck, E. T. Buitenhuis, T. J. Conway, R. Langenfelds, A. Gomez, C. Labuschagne, M. Ramonet, T. Nakazawa, N. Metzl, N. Gillett, and M. Heimann, *Saturation of the Southern Ocean CO2 sink due to recent climate change*, Science, 316 (2007), pp. 1735–1738.

[9] J. Marshall and T. Radko, *Residual-mean solutions for the Antarctic Circumpolar Current and its associated overturning circulation*, Journal of Physical Oceanography, 33 (2003), pp. 2341–2354.

[10] J. Marshall and K. Speer, *Closure of the meridional overturning circulation through Southern Ocean upwelling*, Nature Geoscience, 5 (2012), pp. 171–180.

[11] M. P. Meredith, A. C. N. Garabato, A. M. Hogg, and R. Farneti, *Sensitivity of the Overturning Circulation in the Southern Ocean to Decadal Changes in Wind Forcing*, Journal of Climate, 25 (2012), pp. 99–110.

[12] A. K. Morrison and A. M. Hogg, *On the Relationship between Southern Ocean Overturning and ACC Transport*, Journal of Physical Oceanography, 43 (2013), pp. 140–148.

[13] D. R. Munday, H. L. Johnson, and D. P. Marshall, *Eddy Saturation of Equilibrated Circumpolar Currents*, Journal of Physical Oceanography, 43 (2013), pp. 507–532.

[14] M. Nikurashin and G. Vallis, *A Theory of Deep Stratification and Overturning Circulation in the Ocean*, Journal of Physical Oceanography, 41 (2011), pp. 485–502.

[15] ——, *A Theory of the Interhemispheric Meridional Overturning Circulation and Associated Stratification*, Journal of Physical Oceanography, 42 (2012), pp. 1652–1667.

[16] P. A. O'Gorman and T. Schneider, *Recovery of atmospheric flow statistics in a general circulation model without nonlinear eddy-eddy interactions*, Geophysical Research Letters, 34 (2007).

[17] K. Srinivasan and W. R. Young, *Zonostrophic Instability*, Journal of the Atmospheric Sciences, 69 (2012), pp. 1633–1656.

[18] P. H. Stone, *Baroclinic Adjustment*, Journal of the Atmospheric Sciences, 35 (1978), pp. 561–571.

[19] D. Thompson and S. Solomon, *Interpretation of recent Southern Hemisphere climate change*, Science, 296 (2002), pp. 895–899.

[20] X.-Y. Yang, R. X. Huang, and D. X. Wang, *Decadal changes of wind stress over the Southern Ocean associated with Antarctic ozone depletion*, Journal of Climate, 20 (2007), pp. 3395–3410.